Coincident measurement of the $^{12}C + ^{12}C$ fusion cross section via the differential thick-target technique

W. P. Tan,* A. Gula, K. Lee, A. Majumdar, S. Moylan, O. Olivas-Gomez, Shahina, and M. Wiescher
Department of Physics and Astronomy and Institute for Structure and Nuclear Astrophysics, University of Notre Dame, Notre Dame, Indiana 46556, USA

E. F. Aguilera, D. Lizcano, E. Martinez-Quiroz, and J. C. Morales-Rivera†
Departamento de Aceleradores y Estudio de Materiales, Instituto Nacional de Investigaciones Nucleares, Apartado Postal 18-1027, Codigo Postal 11801, Mexico, D.F., Mexico

(Received 30 May 2024; accepted 3 September 2024; published 16 September 2024)

The $^{12}C + ^{12}C$ fusion reaction is critical for the understanding and interpretation of the late phases of stellar evolution as well as the ignition and nucleosynthesis in cataclysmic binary systems such as type Ia thermonuclear supernovas and x-ray superbursts. Direct measurement of this reaction has been performed at the University of Notre Dame using particle-γ coincidence and differential thick-target techniques with SAND (a silicon detector array) at the high-intensity 5U Pelletron accelerator. Partial cross section results for the channels of p_1 to p_{10} and α_1 at center-of-mass energies of 2.65–5 MeV that are relevant to nuclear astrophysics are reported. The total $S^*(E)$ factor is constructed by taking into account contributions from the missing channels. The recommended reaction rate and its impact on the carbon burning process under astrophysical scenarios will be discussed.

DOI: 10.1103/PhysRevC.110.035808

I. INTRODUCTION

The rate of the $^{12}C + ^{12}C$ fusion reaction is presently one of the most sought-after reaction rates in the study of nuclear astrophysics. This reaction plays a very important role in many different stellar environments such as hydrostatic carbon burning in massive stars [1–3], type Ia thermonuclear supernovas driven by explosive fusion near the core of the white dwarf star in accreting or merging binary systems [4], and x-ray superbursts thought to be ignited by the carbon fusion reactions in the burning ashes of accumulated hydrogen and helium on the surface of accreting neutron stars [5,6]. A recent study has also shown the importance of the $^{12}C + ^{12}C$ reaction rate for the separation of progenitor masses of stars that end their lives as white dwarfs or supernovas [7].

Experimentally it is very challenging to measure the fusion cross section of the $^{12}C + ^{12}C$ system directly due to the dramatic suppression of the cross section by the Coulomb barrier. In the astrophysically important energy range, there are three main particle channels, namely, $^{12}C(^{12}C, p)^{23}Na$ ($Q = 2.241$ MeV), $^{12}C(^{12}C, \alpha)^{20}Ne$ ($Q = 4.617$ MeV), and $^{12}C(^{12}C, n)^{23}Mg$ ($Q = -2.598$ MeV) which can populate the ground state or excited states in the respective residual nuclei that subsequently decay by gamma emission to the ground state. Direct measurement of the neutron-emission channel near astrophysically relevant energies conducted at Notre Dame demonstrated that this channel contributes less than 5% to the total reaction rate [8], similar to the case of the $^{27}Si + n$ channel in the $^{12}C + ^{16}O$ fusion reaction [9]. Experimental effort has thus been concentrated on measurements of the proton and alpha channels of the $^{12}C + ^{12}C$ fusion reaction.

Most of the early experimental efforts following the observation of resonances in the cross section by the Chalk River experiment [10] are direct singles measurements with detection of either charged particles [11–15] or gamma radiation [16–22], some of which are shown in Fig. 1 where the cross section is displayed as the astrophysical $S^*(E)$ factor as defined for fusion reactions between extended nuclei [23]:

$$S^*(E) = \sigma(E)E \exp(87.21/\sqrt{E} + 0.46E) \quad (1)$$

where E is the center-of-mass energy in units of MeV. This approach however requires a reliable unfolding of the cross section data and a correction of the pronounced energy loss effects which are amplified at low energies due to the rapidly declining cross section.

A handicap in the measurement of single particle emission is the background from reactions or elastic scattering of the heavy ion beam particles on target impurities such as deuterium, and single γ spectroscopy could be significantly affected by sodium contamination in the target material. Coincidence techniques between the emitting particles and subsequent γ transitions have been applied to reduce these background contributions and to better identify the specific decay patterns of the ^{24}Mg compound system. The downside of this approach is that it cannot provide measurements for

*Contact author: wtan@nd.edu
†Present address: Facultad de Ciencias, Universidad Autónoma del Estado de México, Instituto Literario 100, Código Postal 50000, Toluca, México.

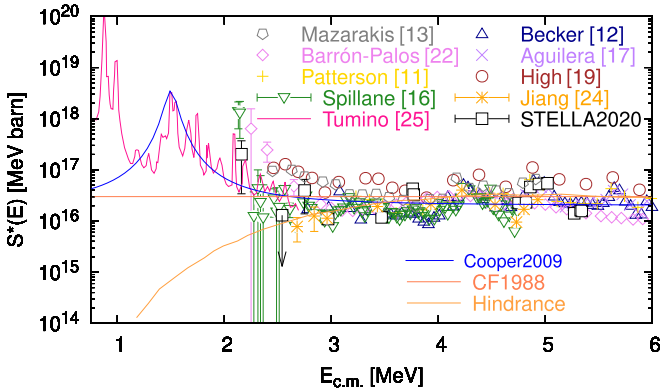

FIG. 1. The total $S^*(E)$ factor data from past measurements [11–13,16,17,19,22,24–26] are shown in comparison with results from the commonly adopted Caughlan-Fowler (CF1988) rate [27] and other models [28,29].

two important channels of p_0 and α_0 that populate the ground states of ^{23}Na and ^{20}Ne, respectively. Nonetheless, it can measure partial cross sections of other open channels very reliably. The most important channels for coincidence measurements are the p_1 transition (emission of protons to the first excited state in ^{23}Na followed by the 440 keV γ transition to the ground state) as well as the α_1 transition (emission of alpha particles to the first excited state in ^{20}Ne with its subsequent ground state decay via the 1634 keV γ transition) as suggested by previous work [12].

An early test experiment using the particle-γ coincidence technique for the $^{12}C+^{12}C$ reaction was conducted at Argonne National Laboratory [30]. Similar techniques were then used to measure the cross sections at a few energies using thin target techniques. These data have been taken at energies below $E_{c.m.} \leqslant 5$ MeV (labeled as "Jiang [24]" and "STELLA2020" [26,31] in Fig. 1). The limited number of data points of these experiments suggests a smooth excitation function but cannot exclude the resonance structures suggested by other works. For "thin" target experiments, the targets should be thin enough relative to the expected width of the resonance structures (typically 100–200 keV in the center-of-mass frame). However, the extracted reaction yields in the previous works (e.g., Refs. [12,24]) have to be averaged over the large energy loss range of a few hundred keV in the target because of the large stopping power of the carbon beam. For example, a 50 (or 70) μg/cm^2 thick carbon target, as used in Refs. [12,24], results in an energy loss of about 360 (or 500) keV for 6 MeV carbon beams. In addition, there is some uncertainty in the target thickness, owing to carbon buildup on the targets during beam bombardment [17]. This can easily cause significant changes of the thickness because of the large energy loss of the impinging ^{12}C particles at low energies.

Despite considerable experimental efforts on direct measurements, the extrapolation towards lower energies, especially below 3 MeV, still carries large uncertainties because of large experimental uncertainties associated with the existing data points and the lack of data at energies below 2.1 MeV. Indirect approaches are therefore necessary to fill the void. One possible approach is to search low energy resonances using the inelastic ^{24}Mg(α,α') reaction [32]. More promisingly, the indirect Trojan Horse method (THM) provided the first set of data at such low energies [25] as shown in Fig. 1. The analysis suggested a number of resonances between $E_{c.m.} = 0.8$ and 2.7 MeV with the overall $S^*(E)$ factor being normalized to the direct data at energies around 2.5 MeV since THM is not able to predict absolute cross section values [33]. The THM data predict a significantly higher reaction rate than all previous estimates. One striking feature is that the resonance structures near 1.5 MeV may provide almost exactly the strength for the reaction rate desired in superburst model simulations [29], as shown in Fig. 1. Unfortunately, the matching strength is not reliable due to the scarcity and large uncertainty of data points from direct measurements that overlap the energy range of the THM results.

However, there is some concern about the analysis of the THM data, in particular with respect to the treatment of Coulomb corrections and the use of the plane wave approximation versus the distorted wave approximation in converting the initial transfer data to $S^*(E)$ factor values [34]. In addition, Coulomb penetrability calculations suggest that the extracted THM resonance strengths are larger than allowed for carbon cluster configurations. Even the base line of the THM $S^*(E)$ factor exceeds the predicted upper limit set by cross sections of $^{12}C+^{13}C$ and $^{13}C+^{13}C$ and M3Y + repulsion coupled-channels calculations [35,36]. The THM $S^*(E)$ factors towards lower energies depend very sensitively on the theoretical analysis.

Extensive theoretical efforts, in particular, in recent years, have also been invested in the determination of the $^{12}C+^{12}C$ reaction rate. The barrier penetration model calculations using the São Paulo potential [37] provide a relatively flat $S^*(E)$ factor ($\approx 5\times10^{16}$ MeV b) at low energies resulting in a reaction rate similar to the widely adopted Caughlan-Fowler (CF1988) rate [27]. However, the possibility of the hindrance effect as shown in Fig. 1, though not confirmed yet, may significantly reduce the $S^*(E)$ factor at energies below 3 MeV leading to a much lower reaction rate [28,38]. A slightly downward trend of the $S^*(E)$ factor at low energies was predicted in a mean field model [39]. More interestingly, resonancelike structures observed in the experimental $^{12}C+^{12}C$ fusion cross section have been qualitatively reproduced by the time-dependent wave-packet method [40] and the antisymmetrized molecular dynamics method [41,42].

Nevertheless, large uncertainties remain in the $^{12}C+^{12}C$ reaction rate especially when extrapolating the data into the astrophysically important energy range (the Gamow window) [3]. The predicted rates depend sensitively on adopted model parameters, hindrance effects, and the possibility of cluster, dynamic, or molecular resonances at relevant energies. Extending and improving the quality of experimental data towards lower energies is therefore crucial for reducing the uncertainties, giving more robust extrapolation towards lower energies, and ultimately providing more reliable reaction rates for the study of carbon burning in stellar environments.

In this paper, we will present a direct measurement of the $^{12}C+^{12}C$ reaction cross sections based on the particle-γ coincidence technique and a target approach that allows us to determine the yield from thin target layers through a

differential thick-target analysis that can potentially address some of the uncertainties present in previous experiments. It is a continuation of the previous work on the same reaction [43] but with better energy coverage, more partial cross section results, and an improved α_1 cross section analysis.

II. EXPERIMENTAL SETUP

A beam of $^{12}C^{2+}$ ions (up to about 14 particle μA) with $E_{\text{c.m.}} = 2.65$–5 MeV, in particular, covering the energy gap of 3–4.1 MeV left in the previous experiment [43], was produced by the single-ended 5U Pelletron accelerator at the Nuclear Science Laboratory (NSL) of the University of Notre Dame. We utilized both particle-γ coincidence and differential thick-target techniques in this paper. The target was a highly ordered pyrolytic graphite (HOPG) [44], which has a layered structure of multiple thin graphene sheets [45]. The advantage of using HOPG as target material is its superior purity compared to natural graphite (e.g., about 1% in impurity of heavy elements that can cause backscattering of the beams in an early test [46]). Impurity of hydrogen and deuterium in the target can cause background in the charged particle spectra [47,48] while impurity of ^{23}Na can severely affect the gamma spectra. The HOPG target with dimensions of 2 cm × 2 cm × 1 mm served also as a water-cooled beam stop. For accurate reading of the beam current, permanent magnets were used and a negative suppression voltage of 1500 V was applied to an isolated graphite ring around the target.

In this paper both charged particles (i.e., protons and alphas) and γ rays emitted from the $^{12}C + ^{12}C$ fusion process were measured simultaneously. The Silicon-Detector Array at Notre Dame (SAND) [9,43] for detection of protons and alpha particles consists of six YY1-type silicon detectors and one S2-type silicon detector [49], covering polar angles from 102° to 146° and 151° to 170° in the laboratory frame. Each wedge-shaped YY1 is segmented into 16 strips on the front junction side with six YY1 detectors forming a "lampshade" configuration. The CD-shaped S2 detector is double-sided and has 48 rings on the front junction side and 16 segments on the back Ohmic side. The solid angle covered by the detectors is 4.1% of 4π for each YY1, and 5.4% of 4π for the S2, as determined from measured and design dimensions in addition to an alpha source calibration. For the measurement of the γ rays, a HPGe detector with relative efficiency of 109% (relative to that of 3 × 3 in. NaI at 1.33 MeV) was placed in a 10 cm thick lead castle and positioned right behind the target to maximize the detection efficiency of γ rays. Radioactive sources of ^{7}Be, ^{56}Co, ^{60}Co, ^{66}Ga, ^{133}Ba, ^{137}Cs, and ^{152}Eu were used to calibrate the HPGe detector for an energy range of 0.1–4.8 MeV. The absolute γ peak efficiency was determined to be 2.30% at 440 keV and 1.22% at 1634 keV with an uncertainty of about 5%. The data were collected by the VME-based digital data acquisition system implemented at NSL, where signals from the silicon detector array and the HPGe detector were processed via MDPP-32 and MDPP-16 digitizers from Mesytec [50]. More details of the setup can be seen in the earlier studies on the $^{12}C + ^{16}O$ and $^{12}C + ^{12}C$ reactions at Notre Dame [9,43].

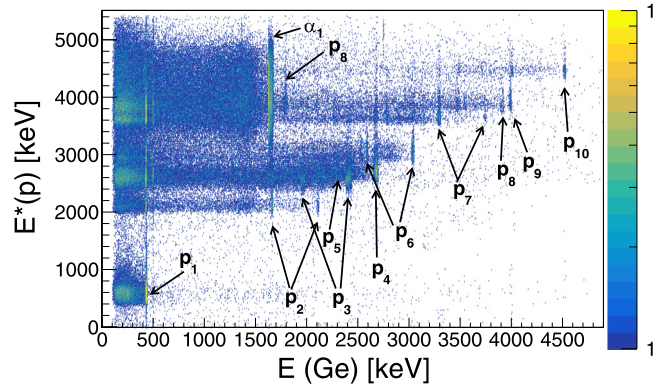

FIG. 2. A coincidence spectrum for a typical run at $E_{\text{beam}} = 8.9$ MeV between charged particles and gamma-rays is shown. Measured particle emitting channels of p_1 to p_{10} and α_1 for the $^{12}C + ^{12}C$ fusion reaction are labeled in the plot.

III. DATA ANALYSIS AND RESULTS

Coincidence data between charged particles and γ rays are shown in Fig. 2 for a typical run at $E_{\text{beam}} = 8.9$ MeV where E(Ge) is the energy of γ rays detected in the HPGe and $E^*(p)$ is the excitation energy of the residual nucleus calculated from the particle energy in SAND after kinematic corrections assumed for the proton channel. Each of the vertical coincident lines corresponding to the labeled channels of p_1 to p_{10} and α_1 also includes feedings at higher $E^*(p)$ values from higher-lying channels, which have to be avoided in the yield determination for individual channels. Background contributions are estimated using the energy bins above the gamma energy for transitions directly to the ground state and the neighboring energy bins for cascading gammas.

The thick-target reaction yield is obtained from the number of events detected per incident carbon nucleus on the target for a given reaction channel. It includes the production yield for reactions not only at the incident beam energy, but also in the energy range below due to the energy loss of beam particles in the thick HOPG target. The obtained thick-target yields for various exit channels from the $^{12}C + ^{12}C$ fusion reaction are depicted in Fig. 3. Particle-γ coincidence

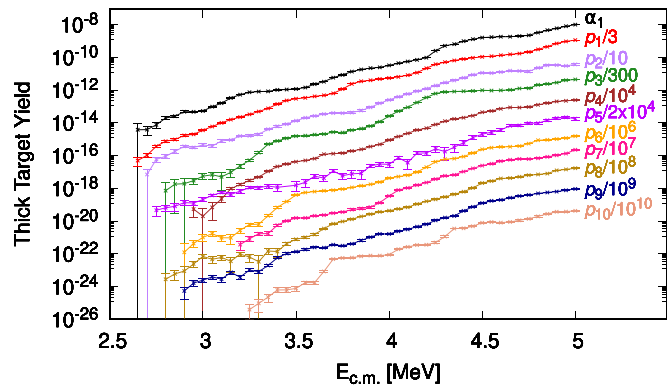

FIG. 3. Thick-target yields are shown for particle emitting channels of p_1 to p_{10} and α_1 for the $^{12}C + ^{12}C$ fusion reaction. For clarity of presentation, the yield of each individual proton channel is scaled down by a factor as indicated in the legend.

TABLE I. Adopted particle-γ coincidence information (from the ENSDF compilation [51]) for the measurement of the $^{12}C + ^{12}C$ reaction channels of p_1 to p_{10} and α_1. E^* refers to the excitation energy of the state with spin and parity of J^π populated by proton or alpha emission, respectively. The subsequent gamma decay information including gamma energy E_γ and decay branching fraction Br(γ) considered for coincidence measurements is also listed.

Channel	E^* (keV)	J^π	E_γ (keV)	Br(γ) (%)
p_1	440.2	5/2+	440.5	100
p_2	2076.2	7/2+	1636.6	91.1
			2076.7	8.9
p_3	2390.9	1/2+	1950.6	34.3
			2390.6	65.7
p_4	2640.5	1/2-	2639.8	100
p_5	2703.8	9/2+	2263.3	62.58
p_6	2982.0	3/2+	2541.3	41.09
			2981.7	58.61
p_7	3677.9	3/2-	3237.2	76.28
			3677.6	2.98
p_8	3847.9	5/2-	1772	60.83
			3848	22.81
p_9	3914.6	5/2+	3914	79.51
p_{10}	4429.63	1/2+	4429.2	90.99
α_1	1633.674	2+	1633.602	100

information for each individual channel including considered gamma decay branching fractions is taken from the ENSDF compilation [51] and listed in Table I. For some high-lying proton channels, not all emitted γ rays are considered and the contributions from missing gamma decays are scaled from their known branching fractions tabulated in Table I. For the α_1 yield, additional contamination from p_2 and other proton channels is subtracted based on the proton yields and the known decay scheme. The gamma detection efficiency, coincidence gate efficiency, solid angle coverage of SAND, and its center-of-mass corrections are applied to obtain the yields.

For clarity, the proton-channel yields in Fig. 3 are divided by a factor as indicated in the plot. The error bars shown in Fig. 3 are statistical. The additional systematic errors are about 5% from the stopping powers [52] and up to about 10% from efficiency calibration and summing effects. We assume isotropic distributions in our measurement which can incur uncertainties of about 10% for p_1 and 30% for α_1 based on previous measurements of angular distributions [12]. However, extreme cases and effects of possible correlations could significantly increase the uncertainties, especially for the α_1 channel [e.g., about 20% for p_1 and 60% for α_1 assuming an angular distribution of $\propto \cos^2(\theta)$].

Another major uncertainty stems from target deterioration with beam accumulation. This translates into a reduction of the reaction yield with beam exposure. The reduction factor is empirically obtained to be 0.98^C for protons and 0.91^C for alphas, where C is the accumulated beam charges in particle Coulombs on the target. This effect is small for proton channels, up to about 20% between the runs from 5 MeV down to 2.7 MeV in the center-of-mass frame, as shown in Fig. 4. However, the effect is much larger for the alpha channel and

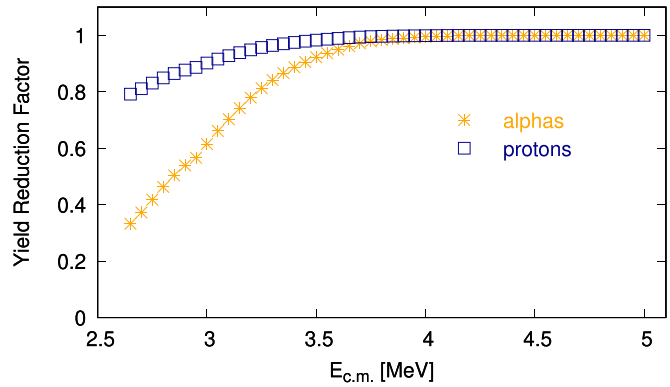

FIG. 4. The yield reduction factors as the energy of the runs are shown for proton and alpha channels due to beam accumulation on the target. As the runs were ordered in decreasing beam energy, beam accumulation and energy were correlated. Therefore, the plot shows the correction factor for each individual run that has to be applied to obtain the thick-target yields shown in Fig. 3.

the reduction factor can be more than three times at the lowest energy point when the most beams are needed for statistics. During the experiment, we stepped down the beam energy strictly in decreasing order as beam charges are accumulated on the target such that the effect of this systematic uncertainty can be minimized, at least in differentiating the yields and therefore preserving the resonance structures.

Such yield reduction factors are explained as follows. HOPG targets have very ordered layers of graphite with high purity. However, beam bombardment can cause HOPG deterioration, that is, bulging structures or buildups surrounding the beam spot become more and more significant as beams are accumulated on the target. The effect, as shown in Fig. 5, is that emitted particles from the fusion reaction could be blocked or scattered by the bulges, especially at less backward angles. It is much more dramatic for alpha particles than protons, especially for runs at energies below 3.5 MeV. From the reaction kinematics, particles emitted at less backward angles are more energetic but still affected more severely by the target conditions as evidenced by Fig. 5, which supports

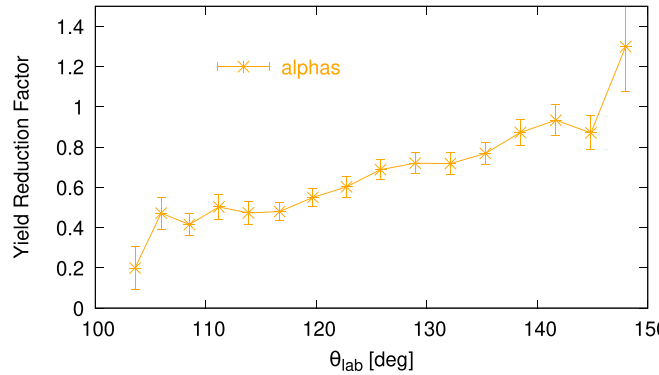

FIG. 5. The measured yield reduction factor for alpha particles is shown as a function of detection angles in the laboratory frame at beam energy of 8.4 MeV after about 6.5-particle-Coulomb beam accumulation on the target.

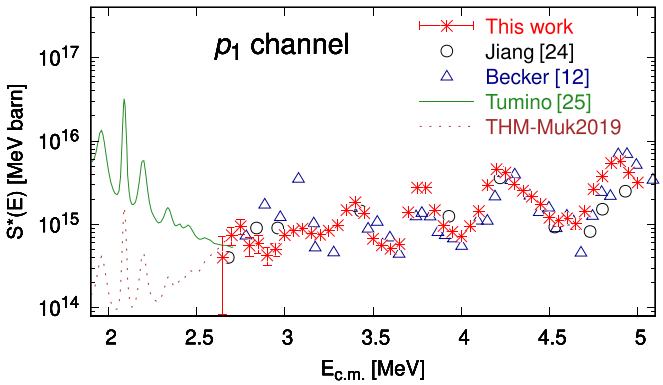

FIG. 6. The p_1 channel $S^*(E)$ factor for this paper is shown and compared with past measurements [12,24,25]. The original THM $S^*(E)$ factor is scaled down by a factor of 10 to match our data.

the bulging assumption. Such target effects are corrected to obtain thick-target yields and corresponding cross sections, contributing mainly to the alpha channel and up to about 30% to the overall systematic uncertainty.

The cross section at the incident energy can then be obtained from the derivative dY/dE of the thick-target yields measured in multiple small energy steps of 50 keV in the center of mass [36]. This makes our effective target thickness ≈50 keV in contrast to a few hundred keV of typical "thin" target experiments [12,24]. The value of dY/dE at a given energy was determined by fitting the yield at this energy together with the yields detected for neighboring energy steps using a second-order polynomial [36]. Whereas this treatment is not possible at the edge of an energy range, a linear fit from one side is applied and results in larger uncertainties for dY/dE. The partial cross sections are derived from the extracted differential yield dY/dE for each of the observed particle groups using the thin target equation:

$$\sigma(E) = \frac{M_T}{f N_A} \frac{dE}{d(\rho X)} \frac{dY}{dE} \tag{2}$$

where f is the molecular fraction of the target nucleus, N_A is the Avogadro constant, M_T is the molecular weight of the target, and $dE/d(\rho X)$ is the stopping power calculated with SRIM [52].

Using the differential thick-target method as presented in Eq. (2), we can obtain the partial cross section. For better comparison and presentation, it is customary to calculate the so-called $S(E)$ factor that removes the strong energy dependence caused by the Coulomb barrier. In particular, we adopt a modified $S^*(E)$ factor for $^{12}C + ^{12}C$ that is commonly used in the literature, as defined in Eq. (1) to take into account the additional finite-size effect of heavy nuclei [23]. Figure 6 shows the p_1 channel $S^*(E)$ factor for this paper in comparison with previous work [12,24,25]. Other data that do not provide separate information on the p_1 channel are not shown. The error bars of our data shown in Fig. 6 are statistical.

The THM p_1 $S^*(E)$ factor (solid line) [25] is scaled down by a factor of 10 to match our data at low energies as presented in Fig. 6. The modified THM-Muk2019 data (dotted line) in consideration of Coulomb interactions as suggested by Ref. [34] are also shown in the figure after normalization to our data is applied. The THM-Muk2019 $S^*(E)$ factor seems to follow the same decreasing trend as the direct data at lower energies. At most energies, our data agree fairly well with the previous direct measurements [12,24] including the resonant structures. At energies right around 3 MeV, the discrepancies with previous work could be due to the detection limit and background issues unavoidable in past singles measurements.

Similarly, new data from other proton channels of p_2 to p_{10} are presented in Fig. 7. In general, our results agree fairly

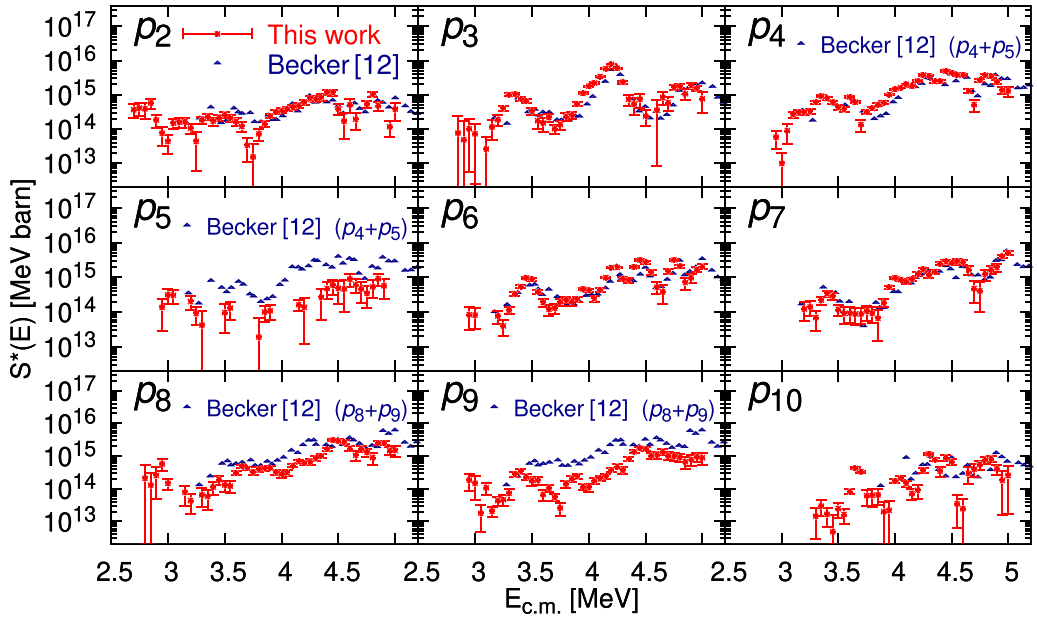

FIG. 7. The $S^*(E)$ factors of p_2-p_{10} channels for this paper are shown and compared with previous work [12]. Note that in Ref. [12], contributions from p_4 and p_5 are not separated and neither are those from p_8 and p_9.

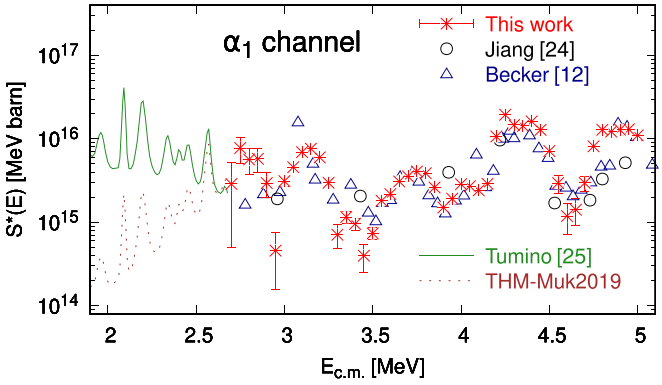

FIG. 8. The α_1 channel $S^*(E)$ factor for this paper is shown and compared with past measurements [12,24,25], where the original THM $S^*(E)$ factor is scaled down by a factor of 4 to match our data at low energies.

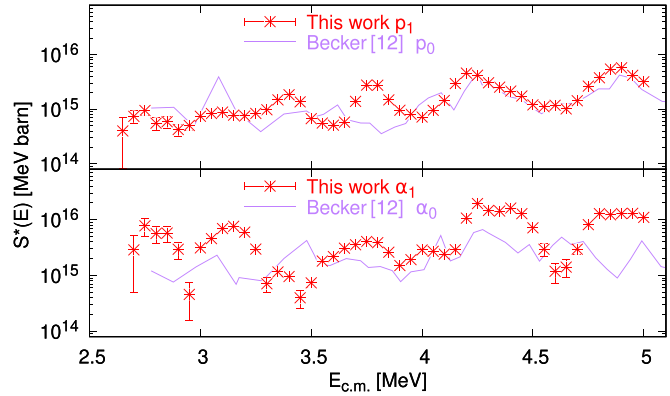

FIG. 9. The p_1 and α_1 $S^*(E)$ factors from this paper are compared with those of important missing channels of p_0 and α_0 taken from the data of Becker *et al.* [12].

well with the data of Becker *et al.* [12]. Again, the trend and resonant structures are consistent between the two data sets. Contributions from all these individual channels are well separated in this paper as shown in Fig. 2. The differences in the channels of p_4, p_5, p_8, and p_9 shown in Fig. 7 are explained as follows. In Ref. [12], singles measurements by detecting only charged particles in silicon detectors showed insufficient energy resolution to separate all individual channels. Therefore, the p_4 and p_5 contributions and the p_8 and p_9 contributions were reported as sums in Ref. [12]. The coincidence technique used in this paper requires the simultaneous detection of gammas in HPGe whose superior energy resolution made it much easier to separate the contributions from these individual channels.

The proton channel data are relatively clean and robust while the alpha data are more prone to background and systematic corrections. As discussed above, contamination from p_2 and higher-lying proton channels has to be subtracted for the α_1 channel. More significantly, the target deterioration that reduces the alpha yields dramatically for runs at $E_{\mathrm{c.m.}} < 3$ MeV must also be taken into account. The resulting α_1 channel $S^*(E)$ factor is shown in Fig. 8 in comparison with previous work [12,24,25]. Keep in mind that the error bars shown in the figure are statistical only and the data may bear large systematic uncertainties, especially at energies of $E_{\mathrm{c.m.}} < 3$ MeV. Nevertheless, the trend and resonant structures from our results are consistent with those of previous direct measurements. Both the original THM α_1 data (solid line) [25] scaled down by a factor of 4 and the THM-Muk2019 $S^*(E)$ factor (dotted line) [34] are also shown for comparison.

To get the total proton $S^*(E)$ factor, we sum up all the partial proton results of p_1–p_{10} and scale it using a linear fit of the ratio $\sum_{i=1}^{10} p_i/p_{\mathrm{total}}$ from the fairly complete data set of Becker *et al.* [12] to take into account other missing channels, especially the p_0 data as presented in Fig. 9. Likewise, we can calculate the total alpha $S^*(E)$ factor using another linear fit of the α_1-to-α_{total} ratio from Ref. [12]. As a result, we obtain the total $S^*(E)$ factor that can be compared to more of the available data in the literature. Unfortunately, such a normalization procedure translates to an uncertainty of up to a factor of 2 due to large fluctuations of the ratios in the data of Becker *et al.* [12]. Nevertheless, our renormalized total $S^*(E)$ factor data (solid circles) are shown in Fig. 10 in comparison with other available data. Note that the two lowest data points of STELLA2020 (one measurement and one upper limit) are taken from their alpha total results since the reported proton total cross sections are much lower (see Supplemental Material [53]).

Our data agree fairly well overall with existing data in the literature although the new $S^*(E)$ factor tends to be lower at lower energies ($E_{\mathrm{c.m.}} < 4$ MeV) in comparison to the previous works possibly due to significant contamination in some of the results of the previous measurements. Meanwhile, our data, consistent with the published thick-target yield of Zickefoose *et al.* [14], agree with the singles measurement from Zickefoose's unpublished thesis work using the thick-target approach [54], which was unfortunately hindered by much larger uncertainty and is therefore not shown in Fig. 10.

IV. CARBON FUSION REACTION RATE

The thermally averaged rate of the $^{12}\mathrm{C}+{}^{12}\mathrm{C}$ fusion reaction in stellar environments can be calculated from [55]

$$\begin{aligned} N_A <\sigma v> &= N_A\left(\frac{8}{\pi\mu}\right)^{1/2}\frac{1}{kT^{3/2}}\int_0^\infty \sigma(E)E \\ &\quad\times \exp\left(-\frac{E}{kT}\right)dE \\ &= \frac{1.5234\times 10^{10}}{T_9^{3/2}}\int_0^\infty S^*(E) \\ &\quad\times \exp\left(-\frac{87.21}{\sqrt{E}} - 0.46E - 11.6045\frac{E}{T_9}\right)dE \end{aligned} \tag{3}$$

where S^* is the modified S factor as defined in Eq. (1), T_9 is the burning temperature in GK, E is the center-of-mass energy in MeV, and the reaction rate is in units of $\mathrm{cm}^3/\mathrm{mol/s}$. To calculate the rate, we adopted the $S^*(E)$ factor in between 2.65 and 5 MeV from this paper. For $E_{\mathrm{c.m.}} = 5$–7 MeV, we used

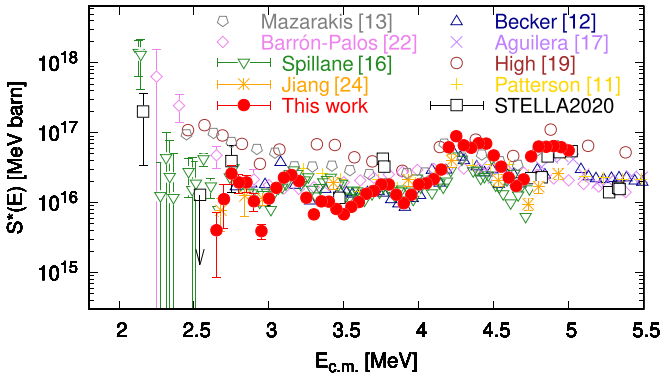

FIG. 10. The total $S^*(E)$ factor for this paper is shown and compared with previous direct measurement data [11–13,16,17,19,22,24,26].

the average $S^*(E)$ factor (orange solid line) from available experimental data sets [12,17,21] as shown in Fig. 11. For $E_{\text{c.m.}} > 7$ MeV, we took the results from Satkowiak *et al.* [18] multiplied by a factor of 1.4 in order to better match the lower energy data. As seen in Fig. 11, this is also a reasonable compromise between two data sets [11,18] at higher energies of $E_{\text{c.m.}} > 7$ MeV.

At lower energies ($E_{\text{c.m.}} < 2.65$ MeV), we applied three options as shown in Fig. 11. The first one is the original THM data [25] with its high energy end normalized to the data of this paper. The second one is to assume a flat S^* factor at lower energies that is taken to be the average of the two lowest energy points of this paper. The last one is the THM-Muk2019 S^* factor due to Coulomb corrections [34] and it is also matched to the direct data of this paper at low energies. Note that the upward trend of the THM option at lower energies is opposite to the downward trend of the THM-Muk2019 option which seems to follow the same trend as our experimental data at lower energies. The three resulting reaction rates are presented in Fig. 12 as ratios to the widely used CF1988 rate [27]. The bumps of the rate ratios at $T_9 \approx 0.2$ and 0.5 reflect resonance structures in the THM S^* factor.

As shown in Fig. 11, the THM-Muk2019 option decreases the S^* factor dramatically at lower energies. The resulting reaction rate as shown in Fig. 12 as a ratio to the CF1988

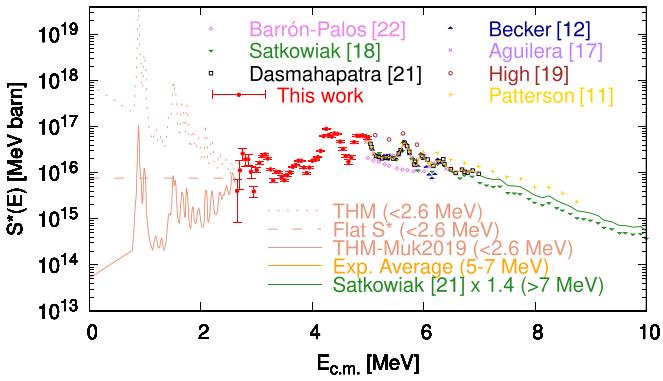

FIG. 11. The total $S^*(E)$ factor adopted for the reaction rate calculations is shown with three different options at lower energies.

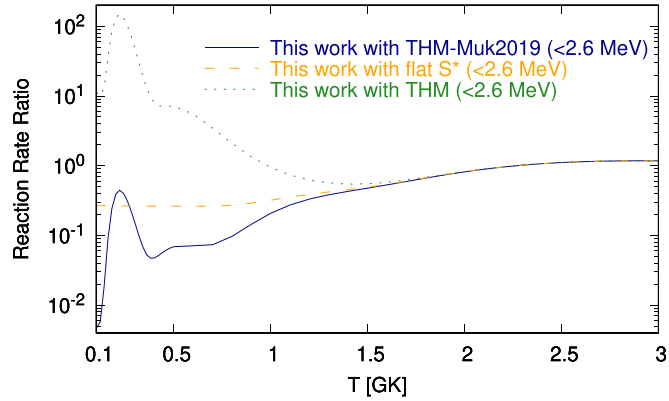

FIG. 12. The reaction rate calculations as ratios to the Caughlan-Fowler (CF1988) rate [27] are shown with three different options of the $S^*(E)$ factor at lower energies.

rate decreases gradually at stellar temperatures $T_9 < 2$. It is reduced by more than an order of magnitude in comparison to the CF88 rate at the superburst temperatures ($T_9 \approx 0.4$–0.5) while also significantly at the hydrostatic burning temperatures ($T_9 \approx 0.6$–1.2). The flat S^* option does not decrease as much but still shows a reduction factor of 3 to 4 at lower temperatures $T_9 < 1$ for the reaction rate. The THM option shows a similarly enhanced reaction rate as the originally reported [25], albeit to a lesser extent by a factor of about 4 due to renormalization to the new data.

V. CONCLUSIONS

Cross section measurements of the $^{12}C + ^{12}C$ fusion reaction were conducted at Notre Dame using particle-γ coincidence and differential thick-target techniques, covering the center-of-mass energy range of 2.65 to 5 MeV. Partial cross sections and corresponding S^* factors were measured for reaction channels of p_1 to p_{10} and α_1. The applied coincidence technique helps minimize possible contamination effects at low energies and the differential thick-target technique can reduce the uncertainty of target thickness integration due to the large energy loss associated with the large stopping power of low energy carbon beams. The new data provide more reliable results on partial cross sections and $S^*(E)$ factors compared to previous measurements. In combination with previous direct and indirect data, the total $S^*(E)$ factor and the reaction rate are calculated using three different options (THM, flat, and THM-Muk2019) at energies below 2.65 MeV by using a normalization factor based on this paper. Further study of this fusion reaction at even lower energies will require more intense beams and less background at a facility such as LUNA-MV at Gran Sasso [56], better particle and gamma detectors with high efficiency coverage, and more stable carbon targets than HOPG.

ACKNOWLEDGMENTS

We would like to thank Edward Stech and Daniel Robertson for their technical support on the operation of the 5U Pelletron accelerator at Notre Dame. We also acknowledge

valuable discussion with Xiaodong Tang, in particular, regarding the beam-target effect on the alpha channel. This work is supported in part by NSF Grants No. PHY-2011890 and No. PHY-2310059 and the Joint Institute for Nuclear Astrophysics (NSF-PFC Grant No. PHY-1430152 and IReNA Grant No. OISE-1927130).

[1] F. Hoyle, Astrophys. J. Suppl. Ser. **1**, 121 (1954).
[2] M. Wiescher, F. Käppeler, and K. Langanke, Annu. Rev. Astron. Astrophys. **50**, 165 (2012).
[3] M. Pignatari, R. Hirschi, M. Wiescher, R. Gallino, M. Bennett, M. Beard, C. Fryer, F. Herwig, G. Rockefeller, and F. X. Timmes, Astrophys. J. **762**, 31 (2013).
[4] W. Hillebrandt and J. C. Niemeyer, Annu. Rev. Astron. Astrophys. **38**, 191 (2000).
[5] E. F. Brown and L. Bildsten, Astrophys. J. **496**, 915 (1998).
[6] E. F. Brown, Astrophys. J. **614**, L57 (2004).
[7] M. Limongi, L. Roberti, A. Chieffi, and K. Nomoto, Astrophys. J. Suppl. Ser. **270**, 29 (2024).
[8] B. Bucher, X. D. Tang, X. Fang, A. Heger, S. Almaraz-Calderon, A. Alongi, A. D. Ayangeakaa, M. Beard, A. Best, J. Browne *et al.*, Phys. Rev. Lett. **114**, 251102 (2015).
[9] X. Fang, W. P. Tan, M. Beard, R. J. deBoer, G. Gilardy, H. Jung, Q. Liu, S. Lyons, D. Robertson, K. Setoodehnia *et al.*, Phys. Rev. C **96**, 045804 (2017).
[10] E. Almqvist, D. A. Bromley, and J. A. Kuehner, Phys. Rev. Lett. **4**, 515 (1960).
[11] J. R. Patterson, H. Winkler, and C. S. Zaidins, Astrophys. J. **157**, 367 (1969).
[12] H. W. Becker, K. U. Kettner, C. Rolfs, and H. P. Trautvetter, Z. Phys. A **303**, 305 (1981).
[13] M. G. Mazarakis and W. E. Stephens, Phys. Rev. C **7**, 1280 (1973).
[14] J. Zickefoose, A. Di Leva, F. Strieder, L. Gialanella, G. Imbriani, N. De Cesare, C. Rolfs, J. Schweitzer, T. Spillane, O. Straniero, and F. Terrasi, Phys. Rev. C **97**, 065806 (2018).
[15] L. Morales-Gallegos, M. Aliotta, L. Gialanella, A. Best, C. G. Bruno, R. Buompane, T. Davinson, M. De Cesare, A. Di Leva, A. D'Onofrio *et al.*, Eur. Phys. J. A **60**, 11 (2024).
[16] T. Spillane, F. Raiola, C. Rolfs, D. Schürmann, F. Strieder, S. Zeng, H.-W. Becker, C. Bordeanu, L. Gialanella, M. Romano, and J. Schweitzer, Phys. Rev. Lett. **98**, 122501 (2007).
[17] E. F. Aguilera, P. Rosales, E. Martinez-Quiroz, G. Murillo, M. Fernández, H. Berdejo, D. Lizcano, A. Gómez-Camacho, R. Policroniades, A. Varela *et al.*, Phys. Rev. C **73**, 064601 (2006).
[18] L. J. Satkowiak, P. A. DeYoung, J. J. Kolata, and M. A. Xapsos, Phys. Rev. C **26**, 2027 (1982).
[19] M. D. High and B. Čujec, Nucl. Phys. A **282**, 181 (1977).
[20] K. U. Kettner, H. Lorenz-Wirzba, and C. Rolfs, Z. Phys. A **298**, 65 (1980).
[21] B. Dasmahapatra, B. Čujec, and F. Lahlou, Nucl. Phys. A **384**, 257 (1982).
[22] L. Barrón-Palos, E. F. Aguilera, J. Aspiazu, A. Huerta, E. Martínez-Quiroz, R. Monroy, E. Moreno, G. Murillo, M. E. Ortiz, R. Policroniades, A. Varela, and E. Chávez, Nucl. Phys. A **779**, 318 (2006).
[23] C. A. Barnes, S. Trentalange, and S.-C. Wu, in *Treatise on Heavy-Ion Science: Volume 6: Astrophysics, Chemistry, and Condensed Matter*, edited by D. A. Bromley (Springer, New York, 1985), Vol. 6, pp. 1–60.
[24] C. L. Jiang, D. Santiago-Gonzalez, S. Almaraz-Calderon, K. E. Rehm, B. B. Back, K. Auranen, M. L. Avila, A. D. Ayangeakaa, S. Bottoni, M. P. Carpenter *et al.*, Phys. Rev. C **97**, 012801(R) (2018).
[25] A. Tumino, C. Spitaleri, M. L. Cognata, S. Cherubini, G. L. Guardo, M. Gulino, S. Hayakawa, I. Indelicato, L. Lamia, H. Petrascu *et al.*, Nature (London) **557**, 687 (2018).
[26] G. Fruet, S. Courtin, M. Heine, D. G. Jenkins, P. Adsley, A. Brown, R. Canavan, W. N. Catford, E. Charon, D. Curien *et al.*, Phys. Rev. Lett. **124**, 192701 (2020).
[27] G. R. Caughlan and W. A. Fowler, At. Data Nucl. Data Tables **40**, 283 (1988).
[28] C. L. Jiang, K. E. Rehm, B. B. Back, and R. V. F. Janssens, Phys. Rev. C **75**, 015803 (2007).
[29] R. L. Cooper, A. W. Steiner, and E. F. Brown, Astrophys. J. **702**, 660 (2009).
[30] C. L. Jiang, K. E. Rehm, X. Fang, X. D. Tang, M. Alcorta, B. B. Back, B. Bucher, P. Collon, C. M. Deibel, B. DiGiovine *et al.*, Nucl. Instrum. Methods Phys. Res., Sect. A **682**, 12 (2012).
[31] M. Heine, S. Courtin, G. Fruet, D. G. Jenkins, L. Morris, D. Montanari, M. Rudigier, P. Adsley, D. Curien, S. Della Negra *et al.*, Nucl. Instrum. Methods Phys. Res., Sect. A **903**, 1 (2018).
[32] P. Adsley, M. Heine, D. G. Jenkins, S. Courtin, R. Neveling, J. W. Brümmer, L. M. Donaldson, N. Y. Kheswa, K. C. W. Li, D. J. Marín-Lámbarri *et al.*, Phys. Rev. Lett. **129**, 102701 (2022).
[33] C. Spitaleri, A. M. Mukhamedzhanov, L. D. Blokhintsev, M. L. Cognata, R. G. Pizzone, and A. Tumino, Phys. Atom. Nuclei **74**, 1725 (2011).
[34] A. M. Mukhamedzhanov, D. Y. Pang, and A. S. Kadyrov, Phys. Rev. C **99**, 064618 (2019).
[35] H. Esbensen, Phys. Rev. C **84**, 064613 (2011).
[36] M. Notani, H. Esbensen, X. Fang, B. Bucher, P. Davies, C. L. Jiang, L. Lamm, C. J. Lin, C. Ma, E. Martin, K. E. Rehm, W. P. Tan, S. Thomas, X. D. Tang, and E. Brown, Phys. Rev. C **85**, 014607 (2012).
[37] L. R. Gasques, A. V. Afanasjev, E. F. Aguilera, M. Beard, L. C. Chamon, P. Ring, M. Wiescher, and D. G. Yakovlev, Phys. Rev. C **72**, 025806 (2005).
[38] L. R. Gasques, E. F. Brown, A. Chieffi, C. L. Jiang, M. Limongi, C. Rolfs, M. Wiescher, and D. G. Yakovlev, Phys. Rev. C **76**, 035802 (2007).
[39] A. Bonasera and J. B. Natowitz, Phys. Rev. C **102**, 061602(R) (2020).
[40] A. Diaz-Torres and M. Wiescher, Phys. Rev. C **97**, 055802 (2018).
[41] Y. Taniguchi and M. Kimura, Phys. Lett. B **823**, 136790 (2021).
[42] Y. Taniguchi and M. Kimura, Phys. Lett. B **849**, 138434 (2024).
[43] W. P. Tan, A. Boeltzig, C. Dulal, R. J. deBoer, B. Frentz, S. Henderson, K. B. Howard, R. Kelmar, J. J. Kolata, J. Long *et al.*, Phys. Rev. Lett. **124**, 192702 (2020).
[44] C. Soldano, A. Mahmood, and E. Dujardin, Carbon **48**, 2127 (2010).
[45] K. S. Novoselov, A. K. Geim, S. V. Morozov, D. Jiang, M. I. Katsnelson, I. V. Grigorieva, S. V. Dubonos, and A. A. Firsov, Nature (London) **438**, 197 (2005).

[46] X. Fang, Measurement and extrapolation of total cross sections of 12C + 16O fusion at stellar energies, Ph.D. thesis, University of Notre Dame, 2016.
[47] L. Morales-Gallegos, M. Aliotta, C. G. Bruno, R. Buompane, T. Davinson, M. D. Cesare, A. D. Leva, A. D'Onofrio, J. G. Duarte, L. R. Gasques *et al.*, Eur. Phys. J. A **54**, 132 (2018).
[48] J. Zickefoose, J. Schweitzer, T. Spillane, F. Strieder, H.-W. Becker, C. Rolfs, A. Di Leva, M. De Cesare, N. De Cesare, F. Terrasi, L. Gialanella, D. Schürmann, Y. Guan, G. Imbriani, and B. Limata, in *Proceedings of 11th Symposium on Nuclei in the Cosmos: PoS(NIC XI)* (Sissa Medialab, Heidelberg, 2011), p. 019.
[49] Micron semiconductor, http://www.micronsemiconductor.co.uk/.
[50] Mesytec, http://www.mesytec.com/.
[51] M. Shamsuzzoha Basunia and A. Chakraborty, Nucl. Data Sheets **171**, 1 (2021).
[52] SRIM code, http://www.srim.org/.
[53] See Supplemental Material at http://link.aps.org/supplemental/10.1103/PhysRevC.110.035808 for more comparisons of the p-total and α-total results.
[54] J. Zickefoose, $^{12}C + ^{12}C$ fusion: Measurement and advances toward the Gamow energy, Ph.D. dissertation, University of Connecticut, 2011.
[55] W. A. Fowler, G. R. Caughlan, and B. A. Zimmerman, Annu. Rev. Astron. Astrophys. **13**, 69 (1975).
[56] P. Prati and LUNA Collaboration, J. Phys.: Conf. Ser. **1342**, 012088 (2020).